RSC Advances

PAPER

View Article Online
View Journal | View Issue

Cite this: *RSC Adv.*, 2018, **8**, 28421

Thermally activated delayed fluorescence processes for Cu(I) complexes in solid-state: a computational study using quantitative prediction†

Lingling Lv, *[a] Kui Liu,[a] Kun Yuan,[a] Yuancheng Zhu[a] and Yongcheng Wang[b]

The photophysical properties of four representative Cu(I) complex crystals have been investigated using the combination of an optimally tuned one- and two-dimensional range-separated hybrid functional (LC-BLYP$^{*}_{\alpha=0.0,\beta=1.0}$ and LC-BLYP$^{**}_{\alpha=0.2,\beta=0.8}$) with the polarizable continuum model, and the thermal vibration correlation function (TVCF) approach. The calculated excited singlet–triplet energy gap, radiative rates and lifetimes match the experimentally available data perfectly. At 300 K, the reverse intersystem crossing (RISC) proceeds at a rate of $k_{RISC}^{dir.} \approx 10^{6-8}$ s^{-1}, which is 4–5 orders of magnitude larger than the mean phosphorescence rate, $k_P \approx 10^{2-3}$ s^{-1}. At the same time, the ISC rate $k_{ISC}^{dir.} \approx 10^{9}$ s^{-1} is again 2 orders of magnitude larger than the fluorescence rate $k_F \approx 10^{7}$ s^{-1}. In the case of $k_{RISC}^{dir.} \gg k_F$ and $k_{RISC}^{dir.} \gg k_P$, thermally activated delayed fluorescence should occur. Vibronic spin–orbit coupling can remarkably enhance the ISC rates by the vital "promoting" modes, which can provide crucial pathways to decay. This can be helpful for designing novel excellent TADF Cu(I) complex materials.

Received 11th June 2018
Accepted 20th July 2018

DOI: 10.1039/c8ra04978e

rsc.li/rsc-advances

1. Introduction

Recently, the thermally activated delayed fluorescence (TADF) materials displayed by organo-transition metal complexes and organic molecules have attracted great attention because of the remarkable variability in their emission properties for organic light-emitting diodes (OLED).[1–4] Under electrical excitation, the singlet–triplet counter pairs of electrons and holes are equally weighted to recombine and yield excitons, resulting in 25% singlet excitons and 75% triplet excitons in the electroluminescence device according to spin statistics.[5–7] However, the energies of all triplet excitons (75%) are dissipated as heat in the conventional fluorescent materials, which leads to a theoretical upper limit of 25% for the internal quantum efficiency (Fig. 1).[6,7] To obtain high-efficiency OLED materials, recent studies have found that TADF emitters can rely on efficient thermal upconversion from the triplet state T_1 into an emissive singlet state S_1 through reverse intersystem crossing (RISC), which in principle, causes the efficiency of exciton utilization to reach 100%.[8–10]

It is well known that efficient TADF must satisfy the vital condition of a small energy gap, $\Delta E(S_1–T_1)$, between the T_1 and S_1 states involved in the RISC process. One effective strategy to decrease the $\Delta E(S_1–T_1)$ involves using covalently linked electron donor and acceptor units and consequently, such molecules have become the focus of molecular designs adopted for TADF.[11] Using this strategy, one obtains the T_1 and S_1 states with strong charge transfer (CT) character from the highest occupied molecular orbital (HOMO) to the lowest unoccupied molecular orbital (LUMO) transitions. These states are characterized by a small spatial overlap between the HOMO and

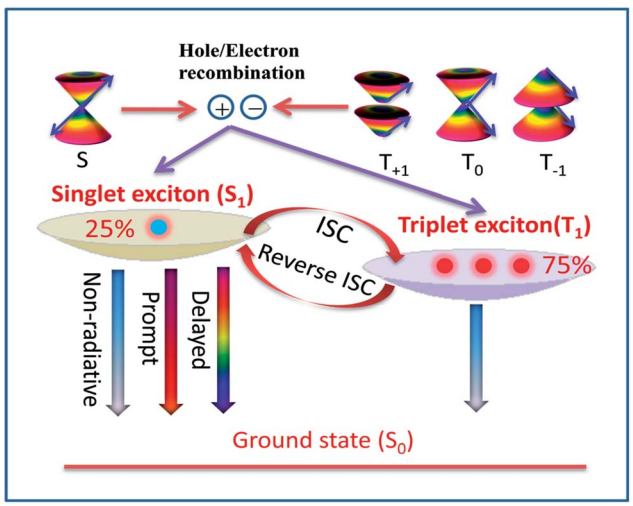

Fig. 1 Diagram of the delayed fluorescence process based on spin-statistics in TADF molecules.

[a]College of Chemical Engineering and Technology, Tianshui Normal University, TianShui, GanSu 741001, China. E-mail: lvling100@163.com
[b]College of Chemistry and Chemical Engineering, Northwest Normal University, LanZhou, GanSu 730070, China. E-mail: ycwang02@163.com

† Electronic supplementary information (ESI) available. See DOI: 10.1039/c8ra04978e

LUMO, which decreases the electron exchange energy and the energy gap, $\Delta E(S_1–T_1)$.[11,12] However, in this simple model, one negative effect is inevitably generated: the small spatial $\langle$HOMO|LUMO$\rangle$ overlap for S_1 with CT causes the slow radiative decay rate of the $S_1 \rightarrow S_0$ transition and low luminescence efficiency. Therefore, it is an essential challenge to obtain a reasonable balance between a small $\Delta E(S_1–T_1)$ and the oscillator strength of the $S_1 \rightarrow S_0$ transition in the TADF molecular design. An accurate evaluation of $\Delta E(S_1–T_1)$ with a reasonable oscillator strength is necessary to guide the TADF molecular design and expand the range of TADF materials.

Moreover, it is well established that the optical properties of TADF materials can have a considerable impact as a function of their environment. In other words, TADF materials are usually mixed into appropriate host matrixes to remit the concentration quenching and exciton annihilation processes, which restrain the efficiency enhancement of OLEDs. The study reported by Yersin *et al.*[13] has shown that the same TADF complex can have a much larger photoluminescence quantum yield in the solid state than that in solution. Therefore, it is also a challenge to be able to accurately describe the solid phase excited-state properties of TADF emitters. However, the theoretical studies of TADF materials, taking into account a solid-state environment, have great limitations so far.

From a theoretical standpoint, a reliable and computationally efficient method for the prediction of the excited state properties for the solid state would thus be highly beneficial since it would allow one to possibly help in determining the origin of the variation in experimental results. The time-dependent density functional theory (TD-DFT) is a useful and reliable tool to compute the excited states of relatively larger systems and is considerably more computationally efficient.[14] Unfortunately, the conventional (semi)local exchange–correlation (XC) functionals may fail completely in predicting the electronic structure in donor–acceptor CT systems.[15] In addition, for molecular crystals, the surrounding environment is substantially different from that of single molecules, ascribed to polarization effects, which is essentially a phenomenon related to nonlocal correlation. These systematic errors are mainly attributed to the inappropriate XC introduction and the potential and density can be incorrect at asymptotically large distances.[16–18] Recently, the range-separated exchange (RS) density functional comprising a suitable fixed amount of exact-exchange (eX) has overcome the incorrect asymptotic behavior in the long-range limit, and provides an improved description of the excited-state properties.[16–21] Abramson *et al.*[22] reported the dielectric constant (ε) in a "screened" RS functional by replacing the $1/R$ asymptotic behavior with the more general asymptotic $1/(\varepsilon \times R)$, which is required when the calculations are performed on the periodic crystals. Very recently, a more computationally efficient method was proposed by Sun *et al.*[23] for the quantitative characterization of the excited-state properties in molecular crystals. This calculation method is to combine the polarizable continuum model (PCM) and optimally tuned RS functionals, whose advantage comes from the optimal tuning of the range-separation parameter ω for a long-range corrected (LC) functional in the PCM environment. For the simulation of a solid-state environment, the molecules in the crystal phase were "dissolved" in a solvent with the same kind of molecules as the crystal.

Potential candidates for Cu(I) complexes in the fields of OLEDs have attracted a lot of attention from the academic and commercial communities. A much deeper investigation of the photophysical and chemical properties of the Cu(I) compounds will lead to the development of new materials and material design strategies. In this study, we chose four representative TADF emitters that are Cu(I) complexes, namely, Cu(pop)(NN) (pop = bis(2-(diphenylphosphanyl)-phenyl)ether and NN = bis(pyrazol-1-yl)borohydrate(pz_2BH_2), tetrakis(pyrazol-1-yl) borate (pz_4B), bis(pyrazol-1-yl)-diphenyl-borate (pz_2Bph_2) and dppb = 1,2-bis(diphenylphosphino)-benzene; Fig. 2), as our research objects because their extensive experimental data are available.[13] Herein, the k_r radiative decay rates are determined *via* the Einstein relationship and the k_{ISC} decay rates are quantitatively calculated using the thermal vibration correlation function (TVCF) rate theory in combination with the PCM-tuned LC-BLYP method in the solid-state.[24–29] In addition, vibronic spin–orbit coupling (SOC) has been taken into account from the promoted vibration modes.

2. Computation details

2.1 Optimization of geometries

The optimal tuning method was performed according to the RS functionals. In the expression of RS hybrid functionals, the two-electron repulsion operator $1/R_{12}$ was divided into a short-range

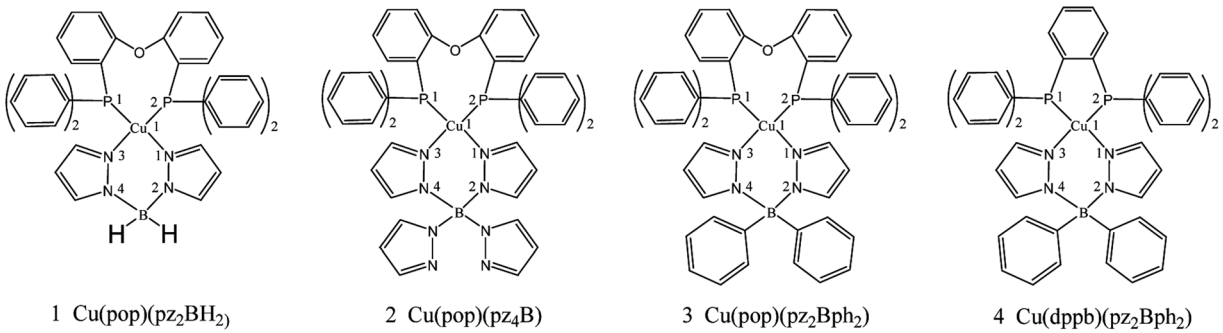

Fig. 2 Chemical structure of mononuclear Cu(I) complexes.

domain and a long-range domain by means of the Ewald-style partition based on the error function (erf) as follows:[30]

$$\frac{1}{R_{12}} = \frac{1-[\alpha+\beta\,\mathrm{erf}(\omega R_{12})]}{R_{12}} + \frac{\alpha+\beta\,\mathrm{erf}(\omega R_{12})}{R_{12}} \quad (1)$$

where R_{12} is the distance between the electrons at the coordinate vectors R_1 and R_2; the range-separation parameter ω (units of bohr^{-1}) determines the ratio between the ranges depending on the value of R_{12}. The first term on the right-hand side in eqn (1) is a short-range interaction described by DFT exchange potential, and the second term is the long-range interaction described by the HF exchange integral. For an asymptotically correct LC functional, $\alpha + \beta = 1$, which is enforced for the optimal tuning in this study. The optimal tuning procedure is based on the exact Kohn–Sham (KS) theory, in which the negative HOMO energy for an N-electron system equals the vertical ionization potential;[23] this expression is as follows:

$$J^2 = \sum_{i=0}^{1} [\varepsilon_H(N+i) + \mathrm{IP}(N+i)]^2 \quad (2)$$

In addition, there have been recent studies[31,32] showing that some amount of short-range HF exchange (*i.e.* setting α to a nonzero value) can lead to improved electronic properties and excitation energies. We used two different parameterizations: a long-range corrected LC-BLYP functional without any short-range exchange (*i.e.*, $\alpha = 0.0$, $\beta = 1.0$) as well as an LC-BLYP functional containing 20% exchange over the entire range (*i.e.*, $\alpha = 0.2$, $\beta = 0.8$) in conjunction with tuning ω *via* the non-empirical procedure,[33] which are denoted as LC-BLYP$^{*}_{\alpha=0.0,\beta=1.0}$ and LC-BLYP$^{**}_{\alpha=0.2,\beta=0.8}$.

The optimization of the parameter ω was performed by tuning the optDFTw procedure,[34] as described in Fig. 3, and all the ground geometries were optimized using the LC-BLYP$^{*}_{\alpha=0.0,\beta=1.0}$ functional and 6-31+G(d) basis set as shown in Fig. 5. The geometries of the excited states were optimized using the corresponding time-dependent TD-LC-BLYP$^{*}_{\alpha=0.0,\beta=1.0}$ functionals. As for the simulation of the environmental solid polarization effects, the default PCM model using the integral equation formalism variant was employed, where the molecule in the crystal phase was "dissolved" in the solvent with the same kind of crystal molecules. These were performed by adding the "SCRF (PCM, solvent = generic, read)" keyword in the Gaussian

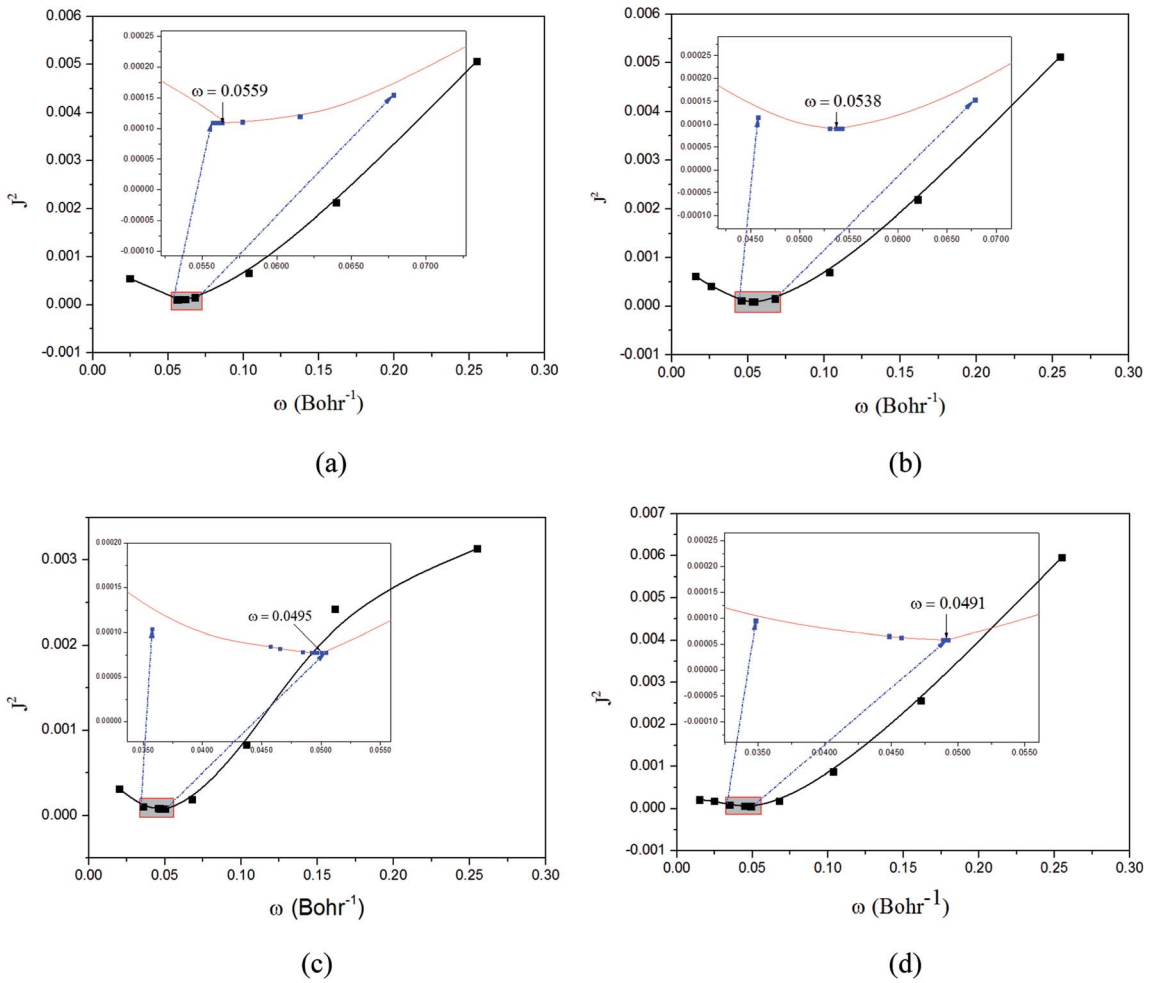

Fig. 3 Functions defined in eqn (2) used for determining of the optimally-tuned range-separation parameter ω (bohr^{-1}) at the LC-BLYP$^{*}_{\alpha=0.0,\beta=1.0}$/6-31 + G(d) level in the solid state. (a) Cu(pop)(pz$_2$BH$_2$); (b) Cu(pop)(pz$_4$B); (c) Cu(pop)(pz$_2$Bph$_2$); (d) Cu(dppb)(pz$_2$Bph$_2$).

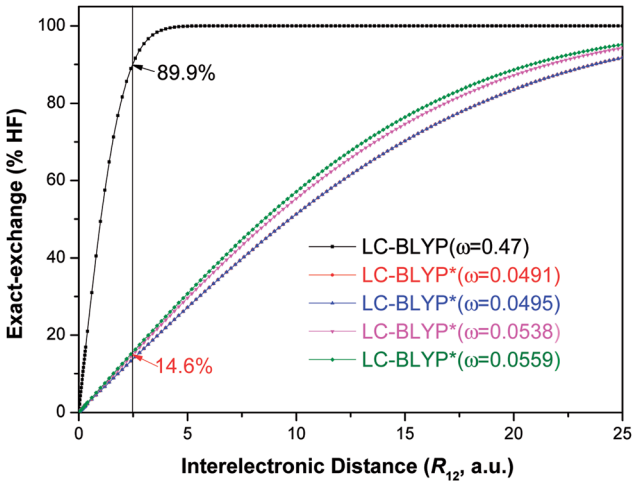

Fig. 4 Diagram of the percentage of exact-exchange (%HF) *versus* the interelectronic distance (R_{12}) for the LC-BLYP$^{*}_{\alpha=0.0,\beta=1.0}$ functional in the four Cu(I) complexes.

09 package.[35] The settings for the PCM parameters have been explicitly described in ref. 23*b*.

2.2 Calculations of the electronic-structure and energy gap $\Delta E(S_1–T_1)$

High level of accuracy of calculations is crucial for the quantitative theoretical prediction of TADF molecules. As described in previous studies, the vertical excitation energies of the $S_0 \rightarrow S_1$, $E_V(S_1)$ and $S_0 \rightarrow T_1$, $E_V(T_1)$ and the energy gap $\Delta E(S_1–T_1) = E_V(S_1) - E_V(T_1)$ were calculated by applying the PCM-tuned TD-LC-BLYP$^{*}_{\alpha=0.0,\beta=1.0}$ and PCM-tuned TD-LC-BLYP$^{**}_{\alpha=0.2,\beta=0.8}$ functionals, combined with the 6-31+G(d) basis set within the Tamm–Dancoff approximation (TDA).[36] For comparison, two exchange–correlation functionals, namely, B3LYP ($\alpha = 0.2$) and M062X ($\alpha = 0.54$), and two RS hybrid functions, CAM-B3LYP ($\omega = 0.33$, $\alpha = 0.19$, $\alpha + \beta = 0.65$) and ωB97XD ($\omega = 0.20$, $\alpha = 0.22$, $\alpha + \beta = 1.0$), were used.[23*b*,25] To give a quantitative characterization of the excited states, we also calculated the distance between the centroid of the hole and electron, $\Delta R_{H–L}$, hole–electron overlap integral $S_{H–L}$, and CT excitation energy E_{CT} corresponding to the $S_0 \rightarrow S_1$ transition. These calculations were conducted at the theoretical level of PCM(ε)-tuned TD-LC-BLYP$^{**}_{\alpha=0.2,\beta=0.8}$/6-31 + G(d) using the Multiwfn program.[37]

2.3 Calculations of fluorescence and phosphorescence rates

The phosphorescence transitions ($T_1 \rightarrow S_0$) are strictly forbidden in the regime of non-relativistic treatment. If the SOC is considered, the pure singlet or triplet becomes a mixed state. In this case, the forbidden emission can borrow dipole activity from spin-allowed transitions ($S_0 \leftrightarrow S_n$ and $T_{1,\varsigma} \leftrightarrow T_{m,\varsigma}$; see eqn (3)) through the perturbation SOC interactions, resulting in the non-zero intensity of transitions.[38] These calculations were performed using the parallel version of the combined PCM-tuned LC-BLYP$^{**}_{\alpha=0.2,\beta=0.8}$ functional and restricted open-shell configuration interaction with the single excitation (DFT/ROCIS) method by the ORCA 4.0 package.[39] DFT/ROCIS calculations with the parameters[40] $c_1 = 0.21$, $c_2 = 0.49$, and $c_3 = 0.29$ were performed using the converged restricted Kohn–Sham functions at the PCM-tuned LC-BLYP$^{**}_{\alpha=0.2,\beta=0.8}$/def2-TZVP(-f) level, together with the auxiliary basis set def2/*J* in order to accelerate the calculations in the framework of the RI approximation. The electric dipole transition, $\mu(S_0 \leftarrow T_{1,\varsigma})$, between T_1 and S_0 becomes allowed and $\mu(S_0 \leftarrow T_{1,\varsigma})$can be expressed as follows:[41,42]

$$\mu(S_0 \leftarrow T_{1,\varsigma}) = \langle S_0|\mu_\alpha|T_{1,\varsigma}\rangle = \sum_n \frac{\langle S_0|\mu_\alpha|S_n\rangle\langle S_n|\hat{H}_{SOC}|T_{1,\varsigma}\rangle}{E(T_{1,\varsigma}) - E(S_n)} + \sum_m \frac{\langle T_{1,\varsigma}|\mu_\alpha|T_m\rangle\langle T_m|\hat{H}_{SOC}|S_0\rangle}{E(T_m) - E(S_0)} \quad (3)$$

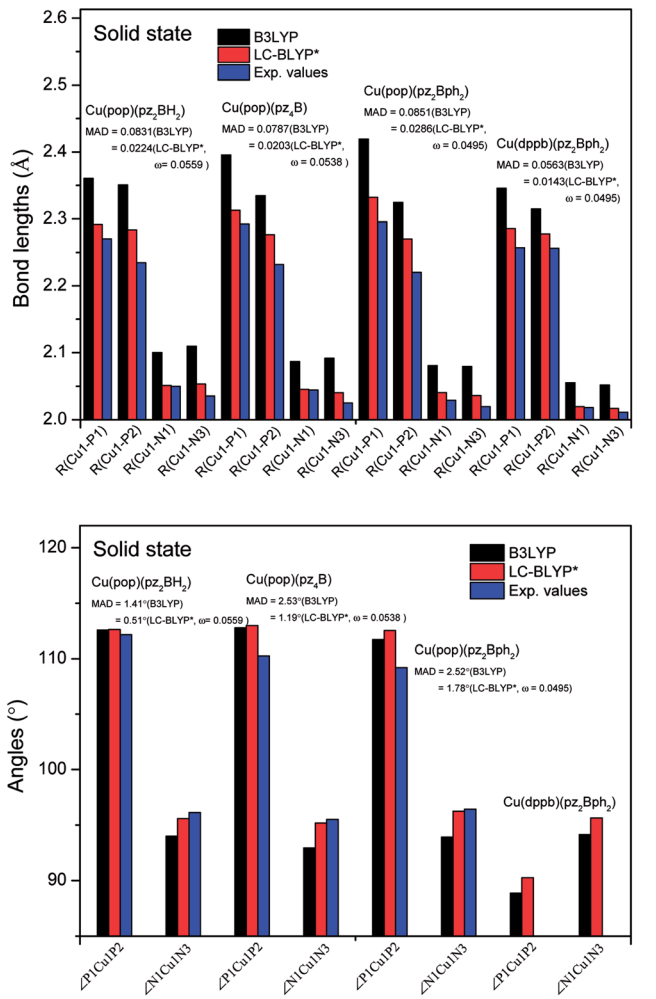

Fig. 5 Calculated mean absolute deviations (MAD) of the vital bond lengths and angles at the equilibrium geometries of the ground state S_0 for the Cu(I) complex molecules in the solid state compared to the experimental values. The MAD values were calculated with respect to the corresponding experimental values, *e.g.* MAD = $1/n\sum_1^n|R_{cal.} - R_{exp.}|$, and LC-BLYP* = LC-BLYP$^{*}_{\alpha=0.0,\beta=1.0}$.

where the operators μ_α and $\hat{H}_{SOC}$ represent the electric dipole and SOC Hamiltonian, respectively. At ambient temperature, the emission rates can be calculated by eqn (4):[41,42]

$$k_{r,\varsigma} = \frac{4e^2}{3c^3\hbar^4}\Delta E^3_{S_0\leftarrow T_{1,\varsigma}}\left|\mu(S_0\leftarrow T_{1,\varsigma})\right|^2 \quad (4)$$

where $\Delta E_{S_0\leftarrow T_{1,\varsigma}}$ indicates a vertical emission energy.

2.4 Calculations of ISC rates

ISC rates of the $T_1 \leftrightarrow S_1$ mainly depend on the energy gap ($\Delta E(S_1–T_1)$) as well as on the strength of the SOC between T_1 and S_1 states. However, in TADF Cu(I) complexes, their SOC interaction is strictly forbidden due to the same CT electronic structures. Therefore, the vibronic SOC contribution to the ISC and RISC rates should be considered,[43] and these calculations were conducted based on the TVCF theory using the MOMAP suite of programs.[24–29] The potential energy surface of S_1 was considered by using $Q_{S1} = SQ_{T1} + D$, relative to that of T_1. The vector D is the displacement between S_1 and T_1 geometries and S is the Duschinsky rotation matrix representing the mixing of normal modes in the S_1 and T_1 states; Q represents the nuclear normal mode coordinates. In the Franck–Condon approximation, the ISC rate constant at temperature T is then given by eqn (5).[26,44]

$$k_{ISC} = \frac{2\pi}{\hbar}|\langle T_1|\hat{H}_{SOC}|S_1\rangle|^2 Z_{T_1}^{-1}\sum_{v,u} e^{-\beta E_v^{T_1}}\left|\langle\Theta_{T_1,v}|\Theta_{S_1,u}\rangle\right|^2 \delta(E_{T_1,v} - E_{S_1,u}) \quad (5)$$

here, $Z_{T_1}^{-1} = \sum_{v=\{0_1,0_2,\ldots,0_N\}}^{\infty} e^{-\beta E_v^{T_1}}$ is the canonical partition function; v and u are the vibrational quantum numbers of T_1 and S_1 states. Further details of the formula can be found in ref. 26.

3. Results and discussion

3.1 Parameter ω optimization and the geometric structures

The optimally tuned derived ω values are given in Fig. 3 for the four Cu(I) molecular systems in the solid states; *i.e.*, using the PCM model with the respective screening effects of the dielectric constant of the molecular crystal during the tuning process. Under the environment of the larger dielectric constants, the optimal ω values were greatly reduced to the range of 0.0491–0.0559 bohr^{-1} for the solid phase system, which is compared with the default $\omega = 0.47$ bohr^{-1} for LC-BLYP. As discussed in detail elsewhere, since ω reflects the global delocalization degree, there is an inverse relationship between the tuned ω value and the spatial extension of the delocalization. The smaller ω values demonstrate that the electron density in the simulated crystal environment is more delocalized than that for the isolated molecule in the gas phase.

In addition, from the perspective of the equation of RS functionals as shown in eqn (1), a smaller ω value corresponds to a larger interelectronic distance, R_{12}, where the description of exchange switches from the short-range DFT-type to the long-range exact-exchange (HF-type) or, in other words, an effective electron delocalization length; the previously optimal ω values were found to decrease with increasing system size and conjugation length. However, in some instances, this correlation was not monotonous and varied strongly for systems with different electronic structures. Here, the Cu(I) complexes have different sizes, being smallest for Cu(pop)(pz_2BH_2) (ω = 0.0559 bohr^{-1}) and largest for Cu(pop)(pz_2Bph_2) ($\omega = 0.0495$ bohr^{-1}) and Cu(dppb)(pz_2Bph_2) ($\omega = 0.0491$ bohr^{-1}), which has a strong dependence of ω on the size of ligands around the central Cu(I) atom.

To illustrate the above behavior, the dependence of the percentage (%HF) of eX in LC-BLYP and LC-BLYP$^*_{\alpha=0.0,\beta=1.0}$ *versus* the R_{12} for four Cu(I) complexes is displayed in Fig. 4. We take the tuned ω value of the LC-BLYP$^*_{\alpha=0.0,\beta=1.0}$ functional for the Cu(dppb)(pz_2Bph_2) system as an example. At $R_{12} = 2.5$ a.u. for the solid state, the HF exchange of the optimally tuned functional is 14.6% ($\omega = 0.0491$ bohr^{-1}), whereas the default LC-BLYP ($\omega = 0.47$ bohr^{-1}) gives more than 89.9% HF exchange. This indicates that the precise description of the solid phase requires the functionals to include less "localized" HF exchange and more "delocalized" DFT-BLYP exchange for the Cu(I) complexes. The eX percentage functional of the other three complexes is similar to that of Cu(dppb)(pz_2Bph_2).

The ground state (S_0) geometries of the solid state molecules were optimized using the optimally tuned functional LC-BLYP$^*_{\alpha=0.0,\beta=1.0}$ and conventional functional B3LYP. These structural parameters are illustrated in Fig. 5 and Table S1 in the ESI.† It is easily noted that the optimal tuning of functionals is very important for the geometric optimization of S_0. For the B3LYP, deviations in the optimized results are much larger. For example, the mean absolute deviations (MADs) in variation between the lower and the upper deviations are 0.0563 Å and 0.0851 Å, respectively, for the bond lengths in the four Cu(I) complexes and between 1.41° and 2.53° for the bond angles, as compared with the crystal data. For the PCM-tuned ($\omega = 0.0559$ bohr^{-1}) LC-BLYP$^*_{\alpha=0.0,\beta=1.0}$ functional, the MADs were merely 0.0224 Å for the bond lengths and 0.51° for the bond angles in the Cu(pop)(pz_2BH_2) complexes; these estimated geometric parameters are in good agreement with experimental crystal data. In this study, we ultimately chose the PCM-tuned (TD-) LC-BLYP$^*_{\alpha=0.0,\beta=1.0}$ level, unless otherwise stated, to optimize the geometry structures (including the S_0, S_1 and T_1 states) of the Cu(I) molecular crystals.

3.2 Energy gap $\Delta E(S_1–T_1)$ and transition properties

A concise summary of all four Cu(I) molecule excited energies obtained by TD-DFT (B3LYP, M062X, ωB97XD, CAM-B3LYP, LC-BLYP$^*_{\alpha=0.0,\beta=1.0}$ and LC-BLYP$^{**}_{\alpha=0.2,\beta=0.8}$) is given in Table 1. Overall, the two RS functionals provide significantly better predictions for the excited state energies and properties than the conventional hybrid functionals. Compared to the experimental $\Delta E(S_1–T_1)$ values, the energy gaps of Cu(I) molecules are most accurately calculated by LC-BLYP$^{**}_{\alpha=0.2,\beta=0.8}$, including some short-range exchange, and least accurately predicted by B3LYP (this can be attributed to the large electron self-interaction error of the B3LYP functional, which spuriously favors the CT character of the excitations). We also found that LC-BLYP$^{**}_{\alpha=0.2,\beta=0.8}$ significantly improves the accuracy of these

Table 1 Calculated vertical excited energies (eV), $E_v(S_1)$ and $E_v(T_1)$, and the corresponding energy difference $\Delta E(S_1–T_1)$ at the S_0 minimum using the different functional methods, and compared to the experimental values[a]

	Cu(pop)(pz_2BH_2)			Cu(pop)(pz_4B)			Cu(pop)(pz_2Bph_2)			Cu(dppb)(pz_2Bph_2)		
Methods	$E_v(S_1)$	$E_v(T_1)$	$\Delta E(S_1–T_1)$	$E_v(S_1)$	$E_v(T_1)$	$\Delta E(S_1–T_1)$	$E_v(S_1)$	$E_v(T_1)$	$\Delta E(S_1–T_1)$	$E_v(S_1)$	$E_v(T_1)$	$\Delta E(S_1–T_1)$
B3LYP	3.34	3.20	0.14(1129)	3.34	3.22	0.12(968)	3.27	3.16	0.11(887)	3.03	2.96	0.07(565)
M062X	4.42	4.10	0.32(2581)	4.43	4.03	0.40(3226)	4.39	4.09	0.30(2420)	3.83	3.54	0.29(2339)
ωB97XD	4.29	3.89	0.40(3226)	4.30	3.89	0.41(3307)	4.26	3.88	0.38(3065)	3.83	3.51	0.32(2580)
CAM-B3LYP	4.28	3.81	0.47(3791)	4.29	3.80	0.49(3952)	4.25	3.80	0.45(3629)	3.81	3.50	0.31(2500)
LC-BLYP$^{*}_{\alpha=0.0,\beta=1.0}$	2.51	2.45	0.06(484)	2.52	2.47	0.05(403)	2.42	2.35	0.07(565)	2.28	2.23	0.05(403)
LC-BLYP$^{**}_{\alpha=0.2,\beta=0.8}$	**3.34**	**3.20**	**0.14(1129)**	**3.35**	**3.22**	**0.13(1048)**	**3.27**	**3.16**	**0.11(887)**	**3.03**	**2.96**	**0.07(565)**

[a] The experimental values of $\Delta E(S_1–T_1)$: 1300, 1000, 800, and 370 cm^{-1} for Cu(pop)(pz_2BH_2), Cu(pop)(pz_4B), Cu(pop)(pz_2Bph_2), and Cu(dppb)(pz_2Bph_2), respectively; vertical excited energies between about 3.35 and 3.99 eV.

excitations in comparison to the LC-BLYP$^{*}_{\alpha=0.0,\beta=1.0}$ results. The calculated values of $\Delta E(S_1–T_1)$, 1129, 1048, 887, and 565 cm^{-1} for the four Cu(I) molecules, namely, Cu(pop)(pz_2BH_2), Cu(pop)(pz_4B), Cu(pop)(pz_2Bph_2), and Cu(dppb)(pz_2Bph_2), are in very good agreement with the measured values of 1300, 1000, 800, and 370 cm^{-1}, respectively in the powder.[14] In the following investigations, LC-BLYP$^{*}_{\alpha=0.2,\beta=0.8}$/6-31 + G(d) was selected to predict the excited state properties, corresponding to optimal ω values listed in Table 2.

For the studied complexes, their first S_1 and T_1 excited states mainly come from the electronic transitions from HOMO to LUMO, and they possess obvious CT character and have the same configurations, ^{1}CT and ^{3}CT (see Fig. 6). Based on the quantum theory, the S_1 and T_1 states are separated by twice the electron exchange energy J, as illustrated in eqn (6) and (7) with ϕ_L and ϕ_H corresponding to the electron (LUMO) and hole (HOMO) orbitals involved in the transitions, respectively. The J value is determined by the spatial separation and overlap integral of ϕ_L and ϕ_H, the higher overlap of HOMO and LUMO and smaller spatial separation lead to higher J and $\Delta E(S_1–T_1)$.[12]

$$\Delta E(S_1–T_1) = E(S_1) - E(T_1) = 2J \quad (6)$$

$$J = \iint \phi^*_H(r_1)\phi_L(r_2)(1/r_1 - r_2)\phi^*_L(r_1)\phi_H(r_2)d_{r_1}d_{r_2} \quad (7)$$

Thus, to gain a quantitative understanding, parameters such as the extent of hole–electron overlap ($S_{H/L}$) and mean separation distance ($\Delta R_{H–L}$) of HOMO and LUMO associated with the S_1 transitions were calculated using the Multiwfn program,[37] and the calculated results are given in Fig. 6. As expected, a correlation between the $\Delta E(S_1–T_1)$ and $S_{H/L}$ was observed for the solid state Cu(I) complexes, except for Cu(dppb)(pz_2Bph_2) and those with a smaller overlap $S_{H/L}$ and therefore a smaller $\Delta E(S_1–T_1)$. The $S_{H/L}$ overlap gradually decreases, 0.1241 > 0.1189 > 0.1119 for Cu(pop)(pz_2BH_2), Cu(pop)(pz_4B), and Cu(pop)(pz_2Bph_2), respectively, and the corresponding $\Delta E(S_1–T_1)$ values also have a decreasing trend with 1129 > 1048 > 887 cm^{-1}. For the S_1 state of Cu(dppb)(pz_2Bph_2) in the solid state ($\varepsilon = 3.66$), the calculated $S_{H/L}$ and $\Delta R_{H–L}$ values are 0.1557 and 3.06 Å, respectively, which indicate that it should have a larger $\Delta E(S_1–T_1)$; however, contrary to the theoretical analysis, it had a smaller $\Delta E(S_1–T_1)$ of 565 cm^{-1}. One key factor is that this does not consider the localisation and spatial confinement of the HOMO–LUMO. This degree of spatial confinement is very crucial, which will alter the coulombic and exchange energies. Indeed, since the S_1 state of Cu(dppb)(pz_2Bph_2) is more delocalised than the three other S_1 excited states, it will exhibit the smallest $\Delta E(S_1–T_1)$. This is not addressed by the relation $\Delta E(S_1–T_1) \propto S_{H/L}$.

An understanding of the degree of spatial confinement can be gained from the energetic gap (E_g) between the HOMO and the LUMO and the CT excitation energy (E_{CT}), which becomes larger with increasing localisation. According to the description, we would consequently expect that the larger E_g and E_{CT} would lead to the larger $\Delta E(S_1–T_1)$ as confinement increases for the Cu(I) complexes and this trend is reflected in Table 2. Here, a clear trend is found and those with a larger E_g and a larger $\Delta E(S_1–T_1)$ are observed.

Table 2 Optimal range-separated parameters ω ($bohr^{-1}$), dielectric constant ε, calculated ionization potential (IP), electron affinity (EA), energetic gap (E_g), CT excitation energy (E_{CT}) of the molecules in the solid phase; energy is in eV

	PCM(ε)-tuned LC-BLYP$^{**}_{\alpha=0.2,\beta=0.8}$/6-31 + G(d)					
Species	ε	ω	IP($-\varepsilon_H$)	EA($-\varepsilon_L$)	E_g	E_{CT}[a]
Cu(pop)(pz_2BH_2)	3.19	0.0169	5.01	0.59	4.42	0.38
Cu(pop)(pz_4B)	3.23	0.0172	5.10	0.68	4.42	0.30
Cu(pop)(pz_2Bph_2)	3.49	0.0144	4.93	0.65	4.28	0.14
Cu(dppb)(pz_2Bph_2)	3.66	0.0131	4.84	0.78	4.06	−0.63

[a] The CT excitation energy: E_{CT} = IP − EA − 1/R; ε_H = HOMO energy, ε_L = LUMO energy.

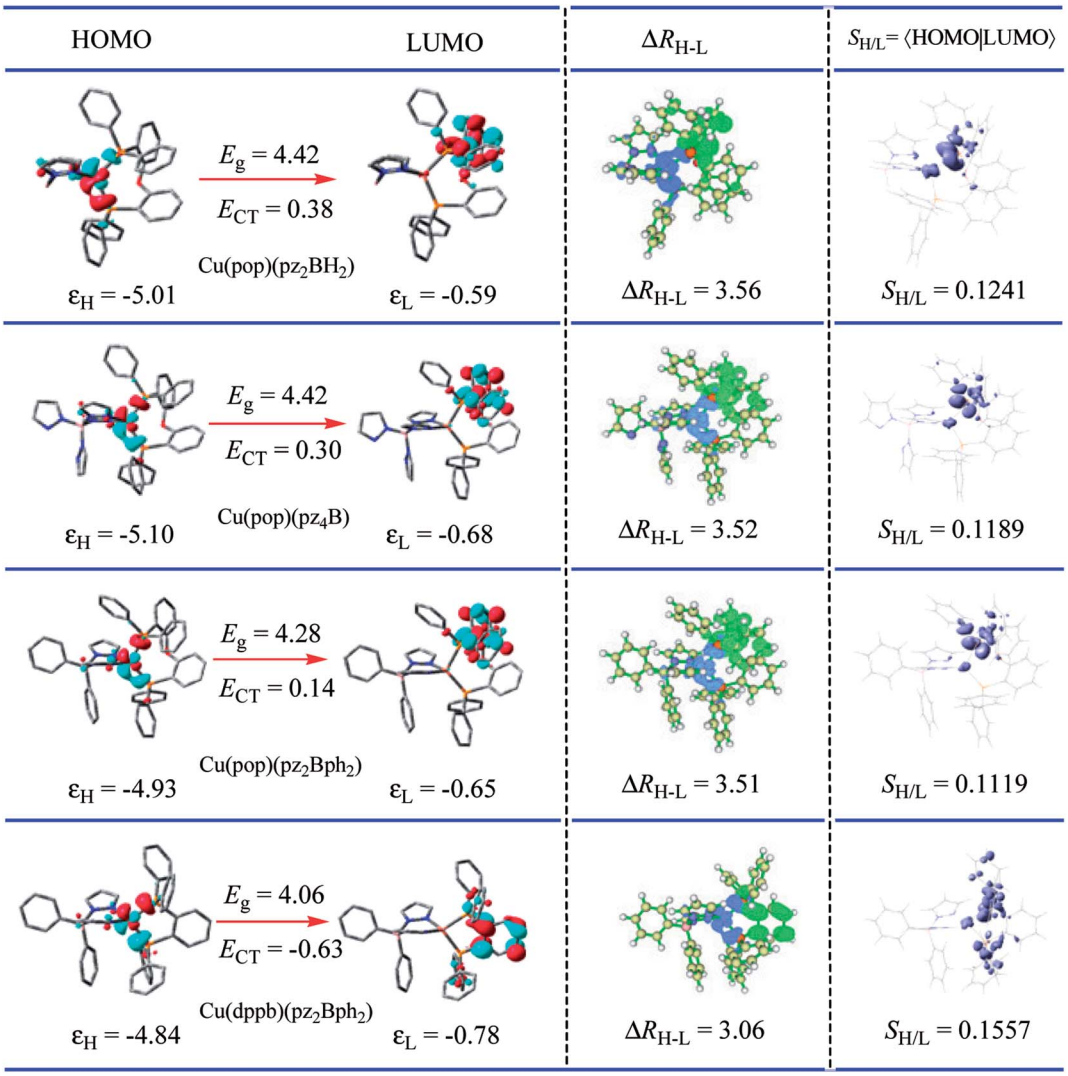

Fig. 6 Computed hole (HOMO)-electron (LUMO) indexes of the mononuclear Cu(I) complexes for selected S_1 states at the PCM(ε)-tuned LC-BLYP$^{**}_{\alpha=0.2,\beta=0.8}$/6-31 + G(d) theoretical level. The distance between the centroid of the hole and electron, ΔR_{H-L} is in Å, the hole–electron overlap integral S_{H-L} is in a.u.; ε_H, HOMO energy; ε_L, LUMO energy; E_g, energetic gap; E_{CT}, CT excitation energy; all energy units are in eV.

3.3 Phosphorescence and fluorescence

For excited T_1 states, if their phosphorescence and non-radiative decay are slow and the energy gap $\Delta E(S_1–T_1)$ is small enough, then after vibration thermalisation, a reverse of ISC back to the S_1 can occur followed by delayed fluorescence; therefore, a detailed study of the T_1 states is very important. We know that the degeneracy of the three spin sublevels ($T_{1,I}$, $T_{1,II}$, and $T_{1,III}$) can be lifted due to the presence of zero-field splitting (ZFS) due to the SOC interaction, which can lead to quite different radiative and non-radiative properties. Yersin *et al.*[13,45] have reported the experimental ZFS values in the range of 1 to 10 cm^{-1} for Cu(I) complex crystals. The results of the

Table 3 Calculated spin–orbit coupling values (cm^{-1}) between T_1 and S_1 for the four Cu(I) complexes and the ZFS tensors D and E with units in cm^{-1}

Species	SOC_x[a]	SOC_y	SOC_z	SOCC[b]	D	E
Cu(pop)(pz$_2$BH$_2$)	−72.74	−58.56	11.07	54.29	4.7	0.1
Cu(pop)(pz$_4$B)	11.52	10.45	13.23	11.78	1.4	0.2
Cu(pop)(pz$_2$Bph$_2$)	−1.18	−1.16	−7.11	4.20	2.6	0.4
Cu(dppb)(pz$_2$Bph$_2$)	−0.50	−2.19	0.12	1.29	0.1	0.0

[a] $SOC_{x,(\text{or } y,z)} = \langle T_1|\hat{H}^{x,(\text{or } y,z)}_{SOC}|S_1\rangle$. [b] $SOCC = \sqrt{(|\langle T_1|\hat{H}^{x}_{SOC}|S_1\rangle|^2 + |\langle T_1|\hat{H}^{y}_{SOC}|S_1\rangle|^2 + |\langle T_1|\hat{H}^{z}_{SOC}|S_1\rangle|^2)/3}$.

Table 4 Computed vertical transition energies ΔE, oscillator strength f, radiative rates k_r, and lifetimes τ of the spin sublevels at the T_1 minimum and the corresponding experimental values in parentheses

State	ΔE (cm^{-1})	f	k_r (s^{-1})	τ (μs)
Cu(pop)(pz_2BH_2)				
$T_{1,I}$	22343.9	1.68×10^{-6}	5.59×10^{2}	1789
$T_{1,II}$	22344.0	9.80×10^{-8}	3.26×10^{1}	30670
$T_{1,III}$	22348.7	6.76×10^{-5}	2.25×10^{4}	44
Average			$k_P = 7.69 \times 10^{3}$	τ_{av} (T_1) = 130 (610)[a]
S_1	22993.3	5.47×10^{-2}	$k_F = 2.89 \times 10^{7}$	τ (S_1) = 0.035 (0.03)[a]
Cu(pop)(pz_4B)				
$T_{1,I}$	22728.3	1.45×10^{-6}	5.28×10^{2}	1894
$T_{1,II}$	22728.5	8.28×10^{-7}	2.85×10^{2}	3509
$T_{1,III}$	22729.9	1.09×10^{-5}	3.75×10^{3}	267
Average			$k_P = 1.53 \times 10^{3}$	τ_{av} (T_1) = 654 (450)[a]
S_1	23200.0	1.06×10^{-2}	$k_F = 3.80 \times 10^{6}$	τ (S_1) = 0.263 (0.2)[a]
Cu(pop)(pz_2Bph_2)				
$T_{1,I}$	20643.3	4.07×10^{-6}	1.16×10^{3}	862
$T_{1,II}$	20643.7	1.58×10^{-5}	4.49×10^{3}	223
$T_{1,III}$	20646.3	1.40×10^{-6}	3.98×10^{2}	2513
Average			$k_P = 2.02 \times 10^{3}$	τ_{av} (T_1) = 495 (480)[a]
S_1	21380.5	3.44×10^{-2}	$k_F = 1.05 \times 10^{7}$	τ (S_1) = 0.095 (0.12)[a]
Cu(dppb)(pz_2Bph_2)				
$T_{1,I}$	22576.1	2.43×10^{-7}	8.26×10^{1}	12106
$T_{1,II}$	22576.1	1.73×10^{-6}	5.88×10^{2}	1701
$T_{1,III}$	22576.2	5.96×10^{-6}	2.03×10^{3}	493
Average			$k_P = 9.01 \times 10^{2}$	τ_{av} (T_1) = 1109(1200)[b]
S_1	22948.66	2.28×10^{-2}	$k_F = 8.06 \times 10^{6}$	τ (S_1) = 0.124 (0.18)[b]

[a] ref. 13*a*. [b] ref. 13*b*.

calculated ZFS parameters show that the D values are in the range of 0.1 to 4.7 cm^{-1} at the PCM-tuned LC-BLYP$^{**}_{\alpha=0.2,\beta=0.8}$/ROCIS/def2-TZVP(-f) levels, consistent with the experimental values (see Table 3).

Taking into account ZFS, k_P (phosphorescence) and k_F (fluorescence) rates or (τ) lifetimes, have been obtained by the PCM-tuned LC-BLYP$^{**}_{\alpha=0.2,\beta=0.8}$/ROCIS/def2-TZVP(-f) calculation at the T_1 geometry, including SOC interactions, which are listed in Table 4. At room temperature, due to the usually small ZFS for the four Cu(I) complexes, an average emission decay time τ_{av} of the three sub-states can be calculated by the three individual decay times according to $\tau_{av} = 3(\tau_I^{-1} + \tau_{II}^{-1} + \tau_{III}^{-1})^{-1}$ (where τ_I, τ_{II}, and τ_{III} represent the emission decay times of the T_I, T_{II}, and T_{III} substates, respectively).[43] The phosphorescence of the four Cu(I) complexes started from T_1 and all the average radiative decay rate constants k_P are relatively slow (less than 10^3 s^{-1}), particularly for Cu(dppb)(pz_2Bph_2), for which the k_P was calculated to be 9.01×10^2 s^{-1} because the decreased rigidity of the dppb ligand leads to a smaller k_P in comparison with the three Cu(I) molecules, including the pop ligand. The calculated means for the three phosphorescence rates are $k_{P,av} = 7.69 \times 10^3$ ($\tau_{av} = 130$ μs), 1.53×10^3 ($\tau_{av} = 654$ μs), 2.02×10^2 ($\tau_{av} = 495$ μs), and 9.01×10^2 s^{-1} ($\tau_{av} = 1109$ μs) for Cu(pop)(pz_2BH_2), Cu(pop)(pz_4B), Cu(pop)(pz_2Bph_2) and Cu(dppb)(pz_2Bph_2), respectively, and the corresponding fluorescence rates k_F (see Table 4) are in good agreement with the experimentally observed values.

3.4 ISC and RISC

As discussed previously, owing to the small energy gap $\Delta E(S_1$–$T_1)$ between the S_1 and T_1, TADF should, in principle, be possible. However, to actually take place effectively, S_1 has to be repopulated, which indicates that the RISC rate should be larger than the rates of radiative and nonradiative decay of the T_1 state to the S_0 state. In fact, the S_1 and T_1 states have the same electronic configurations and almost equivalent weights, and their direct SOC interaction is almost forbidden. In this case, vibronic spin–orbit coupling effects should be considered.

Intersystem crossing rate constants were calculated by considering the direct spin–orbit coupling, ($k^{dir.}_{ISC/RISC}$) and the vibronic spin–orbit coupling, ($k^{vib.}_{ISC/RISC}$) between the T_1 and S_1 states, as shown in Table 5. As can be seen from Tables 4 and 5, for the four Cu(I) complexes, RISC rates are approximately $k^{dir.}_{RISC} \approx 10^{6-8}$ s^{-1} at 300 K, which is 4–5 orders of magnitude

Table 5 Calculated intersystem crossing rate constants (s^{-1}) considering the direct spin–orbit coupling, ($k^{dir.}_{ISC/RISC}$) and the vibronic spin–orbit coupling, ($k^{vib.}_{ISC/RISC}$) between the T_1 and S_1 states, respectively

$T = 300$ K	$k^{dir.}_{ISC}$	$k^{dir.}_{RISC}$	$k^{vib.}_{ISC}$	$k^{vib.}_{RISC}$
Cu(pop)(pz_2BH_2)	4.72×10^9	6.97×10^6	1.39×10^{11}	1.97×10^8
Cu(pop)(pz_4B)	5.68×10^9	1.23×10^7	1.74×10^{10}	3.79×10^7
Cu(pop)(pz_2Bph_2)	6.14×10^9	2.93×10^7	7.94×10^{11}	3.78×10^9
Cu(dppb)(pz_2Bph_2)	1.57×10^9	1.04×10^8	4.85×10^{11}	1.08×10^{10}

larger than the mean phosphorescence rate, $k_P \approx 10^{2-3}$ s^{-1}. This indicates that the S_1 state can be redistributed from the T_1 state by the RISC process. At the same time, the ISC rate $k_{ISC}^{dir.} \approx 10^9$ s^{-1} is again 2 orders of magnitude larger than the fluorescence rate $k_F \approx 10^7$ s^{-1}. Based on the kinetic analysis of a three-level system proposed by Kirchhoff *et al.*,[46] in the case of $k_{ISC}^{dir.} > k_F + k_{IC0}$ and $k_{RISC}^{dir.} > k_P + k_{ISC0}$, the S_1 and T_1 state populations rapidly equilibrate before decaying radiatively at room temperature, and TADF should be observable. Here, the rate constants of the internal conversion of S_1 to S_0 (k_{IC0}) and of ISC from T_1 to S_0 were not calculated owing to the larger energy difference between S_1 (or T_1) and S_0, assuming that these processes are much slower than the radiative rates and will be omitted in the following discussion.

The first equilibrium condition, $k_{ISC}^{dir.} \gg k_F$ is easily satisfied at all temperatures, while the second condition, namely $k_{RISC}^{dir.} \gg k_P$, because of the strong dependence on temperature, is not. A spin-forbidden $T_1 \leftrightarrow S_1$ transition requires the effect of SOC that provides a major mechanism for RISC. SOC induces a different spin-multiplicity mixing that allows the wave function to break spin symmetry, but direct SOC between S_1 and T_1 states tends to zero; thus, a kind of geometrical alteration must exist, which either leads to the increase in the spin–orbit interaction or causes direct T_1–S_1 intersection. For the T_1 state, among many vibration modes, only a few vibration modes play a significant role in altering the geometric structure, inducing stronger SOC interaction. In the present study, these favorite modes are called "promoting" modes, which are determined by Huang-Rhys factors and related reorganization energies of the normal modes, i (see Table S2 in ESI†). Their relationship can be expressed as follows:[47]

$$\lambda = \sum \lambda_i = \sum h\omega_i S_i; \quad S_i = \omega_i D_i^2/2h \tag{8}$$

where S_i and ω_i represent the Huang-Rhys factor and the vibrational frequency for the ith normal mode, respectively; D_i is the coordinate displacement along the mode i. The extent of geometry relaxation between T_1 and S_1 states can be measured by the value of the Huang-Rhys factor. Here, taking the Cu(dppb)(pz_2Bph_2) complex as an example, the calculated S_i and λ_i *versus* the normal mode i on the corresponding S_1 and T_1 potential surfaces are plotted in Fig. 7; those of the remaining complexes are given in Fig. S2–S4 in the ESI.† We noted that

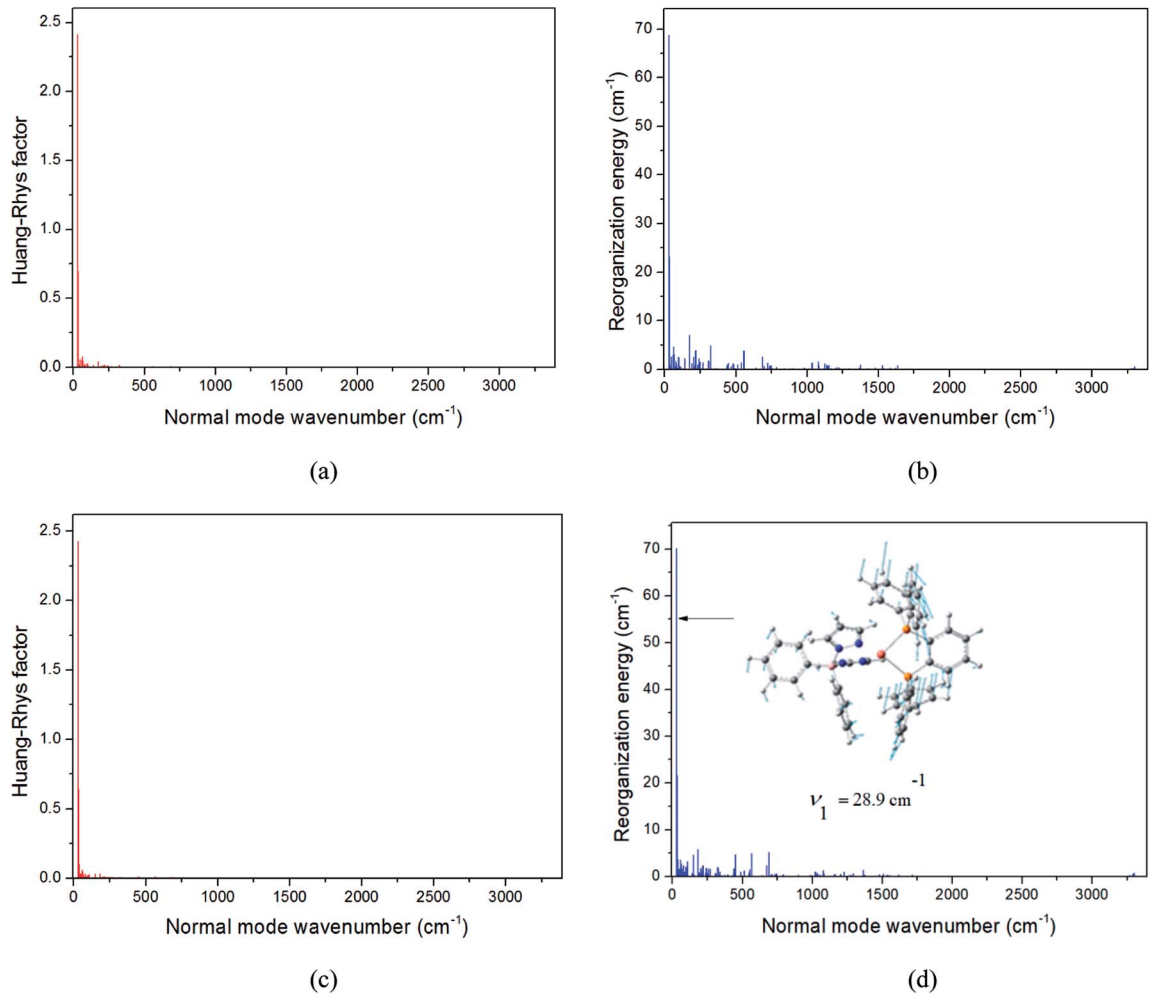

Fig. 7 Calculated Huang-Rhys factors and reorganization energies of each normal mode on the corresponding S_1 (a and b, red) and T_1 (c and d, blue) potential surfaces for Cu(dppb)(pz_2Bph_2). The biggest displacement vector is depicted.

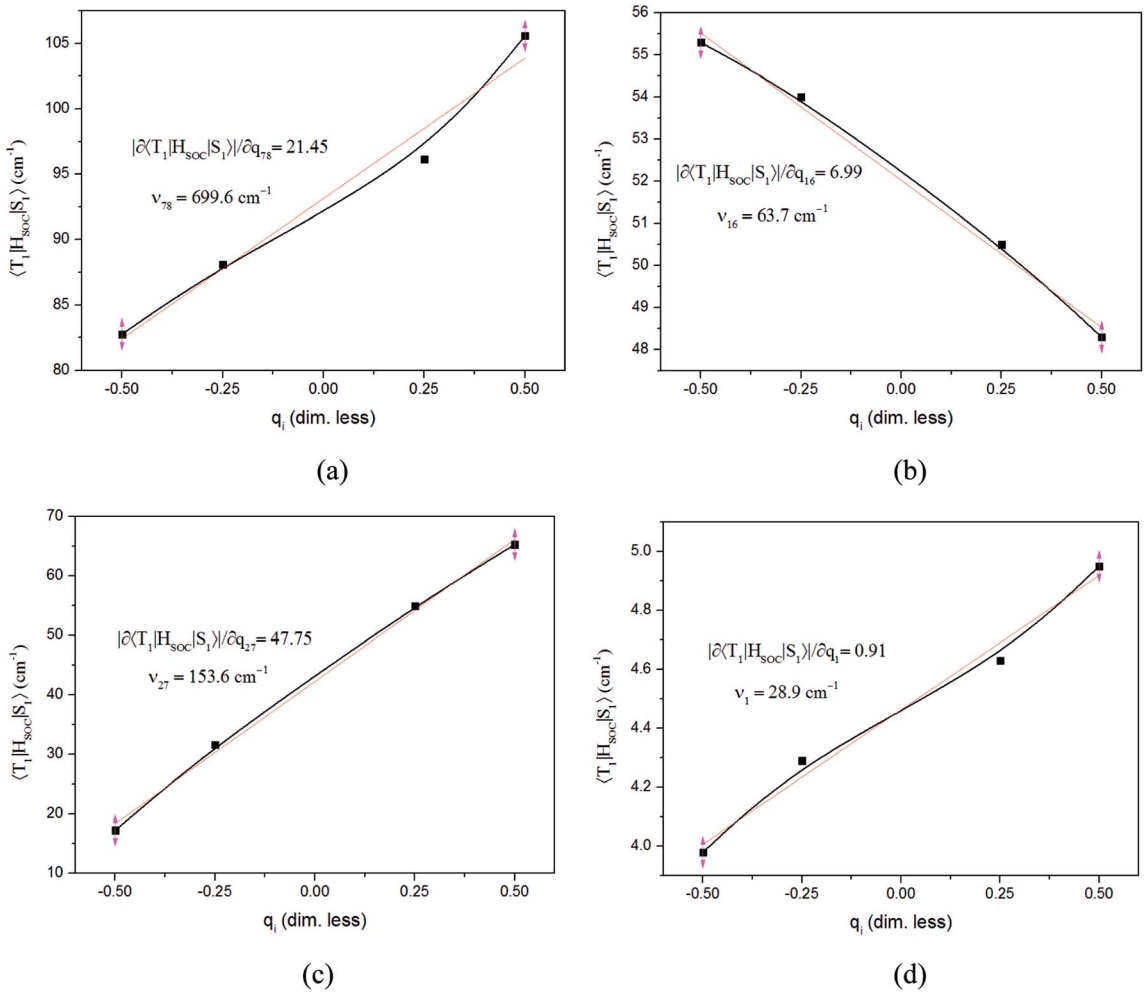

Fig. 8 Change in the SOC ($\langle T_1|H_{SOC}|S_1\rangle$) upon deformation of the vital promoting vibrational normal modes in the triplet state surfaces for the RISC processes. Derivatives of SOCs with respect to the corresponding (dimensionless) coordinates at the equilibrium geometry, $|\partial\langle T_1|H_{SOC}|S_1\rangle|\partial q_i$, and the vibrational normal frequencies, ν_i, are inserted in the box. (a) Cu(pop)(pz_2BH_2); (b) Cu(pop)(pz_4B); (c) Cu(pop)(pz_2Bph_2); (d) Cu(dppb)(pz_2Bph_2).

some low-frequency vibration modes have larger S_i, and one of these vibration frequencies has the largest Huang-Rhys factor and reorganization energy, *i.e.*, it is that vital "promoting" mode, which corresponds to the distortion motion of the phenylene ring of the dppb ligand (see Fig. 7d). This implies that the distortion rotation of the phenylene ring can provide an important channel for conversion between T_1 and S_1.

The values of component-averaged $\langle T_1|H_{SOC}|S_1\rangle$ SOCs calculated along the displacement of the vital "promoting" modes with respect to the coordinates at the equilibrium geometry are illustrated in Fig. 8. For Cu(pop)(pz_2BH_2), Cu(pop)(pz_4B), Cu(pop)(pz_2Bph_2) and Cu(dppb)(pz_2Bph_2), the promoting modes ν_{78}, ν_{16}, ν_{27}, and ν_1 with frequencies of 699.6, 63.7, 153.6 and 28.9 cm^{-1}, corresponding to Huang-Rhys factors S_i = 2.07, 1.07, 4.27, and 2.42 (see Table S2 in ESI†), respectively, lead to the remarkable increase in the $\langle T_1|H_{SOC}|S_1\rangle$ SOCs in the ranges of 82.5–105.2, 48.5–55.3, 16.2–65.3, and 4.0–4.9 cm^{-1}, respectively. Recalling that we calculated the direct SOC to be several orders of magnitude lower, the vibronic SOC may thus be suspected to be the dominant coupling interaction here. The results show that vibronic SOC can remarkably enhance the ISC rates between T_1 and S_1. The largest ISC rates, $k_{ISC}^{vib.}$, including vibronic SOC, were actually obtained for the non-radiative transition $T_1 \leftrightarrow S_1$ and were of the order of $\approx 10^{10-11}$ s^{-1}, which is about 2 orders of magnitude larger than $k_{ISC}^{dir.}$. Moreover, the RISC rates from T_1 to S_1 are affected by the same intensity. Therefore, considering the case of the vibronic SOC, TADF should be obviously observable.

4. Conclusions

The accuracy of the calculation level is crucial for the quantitative theoretical prediction of the photophysical properties of TADF molecules. In this study, the geometries and photophysical properties of a series of TADF Cu(I) crystal complexes have been quantitatively investigated using a methodology proposed by Sun *et al.* This method uses the combination of an optimally tuned one- and two-dimensional range-separated

hybrid functional ($LC\text{-}BLYP^{*}_{\alpha=0.0,\beta=1.0}$ and $LC\text{-}BLYP^{**}_{\alpha=0.2,\beta=0.8}$) with the polarizable continuum model, in which the solid-state screening effects are achieved *via* the introduction of the solid-state dielectric constant, ε. When using an optimal tuning ω value, we find that the LC technique gives an outstanding description of the charge-transfer excited state properties. The calculated results have demonstrated that the two-dimensional tuning of the $LC\text{-}BLYP^{**}_{\alpha=0.2,\beta=0.8}$ functional provides excellent agreement with experimental data. In contrast, we find that reoptimizing the fraction of the Hartree Fock exchange in conventional hybrid functionals still yields an inconsistent description of excitation energies. For geometries, the one-dimensional tuning of the range-separated hybrid functional $LC\text{-}BLYP^{*}_{\alpha=0.0,\beta=1.0}$ performs slightly better than both the B3LYP and $LC\text{-}BLYP^{**}_{\alpha=0.2,\beta=0.8}$ functionals.

Photophysical radiation and non-radiation processes by combining an optimal tuning ω value of LC functional methods and TVCF rate theory have been comprehensively investigated for four Cu(I) complexes. At 300 K, the RISC rate was $k^{\mathrm{dir.}}_{\mathrm{RISC}} \approx 10^{6-8}\ \mathrm{s}^{-1}$, which is 4–5 orders of magnitude larger than the mean phosphorescence rate, $k_{\mathrm{P}} \approx 10^{2-3}\ \mathrm{s}^{-1}$. This indicates that the S_1 state can be redistributed from the T_1 state by the RISC process. At the same time, the ISC rate $k^{\mathrm{dir.}}_{\mathrm{ISC}} \approx 10^{9}\ \mathrm{s}^{-1}$ was again 2 orders of magnitude larger than the fluorescence rate $k_{\mathrm{F}} \approx 10^{7}\ \mathrm{s}^{-1}$. In the case of $k^{\mathrm{dir.}}_{\mathrm{ISC}} \gg k_{\mathrm{F}}$ and $k^{\mathrm{dir.}}_{\mathrm{RISC}} \gg k_{\mathrm{P}}$, the TADF phenomenon should be observable. Hence, the electronic-vibrational coupling activated by temperature is responsible for the occurrence of delayed fluorescence in Cu(I) complexes. It is worth noting that vibronic spin–orbit coupling can remarkably enhance the ISC rates between T_1 and S_1 by the vital "promoting" modes with the larger Huang-Rhys factor. These "promoting" modes correspond to the distortion motion of the phenylene ring of the pop or dppb ligands, which can provide an important pathway to decay between T_1 and S_1, and would be helpful for designing excellent novel TADF Cu(I) complex materials.

Conflicts of interest

There are no conflicts to declare.

Acknowledgements

The study was supported by the National Natural Science Foundation of China (Grant No. 21263022, 21663025, 21663024). We gratefully thank Dr Haitao Sun (East China Normal Universty) for providing the help in using the PCM-tuned LC-BLYP* approach.

References

1 H. Xu, R. F. Chen, Q. Sun, W. Lai, Q. Q. Su, W. Huang and X. G. Liu, *Chem. Soc. Rev.*, 2014, **43**, 3259–3302.
2 Z. Y. Yang, Z. Mao, Z. L. Xie, Y. Zhang, S. W. Liu, J. Zhao, J. R. Xu, Z. G. Chi and M. P. Aldred, *Chem. Soc. Rev.*, 2017, **46**, 915–1016.
3 Y. Tao, K. Yuan, T. Chen, P. Xu, H. H. Li, R. F. Chen, C. Zheng, L. Zhang and W. Huang, *Adv. Mater.*, 2014, **47**, 7931–7956.
4 H. Yersin, A. F. Rausch, R. Czerwieniec, T. Hofbeck and T. Fischer, *Coord. Chem. Rev.*, 2011, **225**, 2622–2652.
5 T. Ogiwara, Y. Wakikawa and T. Ikoma, *J. Phys. Chem. A*, 2015, **119**, 3415–3418.
6 M. A. Baldo, D. O'brien, Y. You, A. Shoustikov, S. Sibley, M. Thompson and S. Forrest, *Nature*, 1998, **395**, 151–154.
7 F. B. Dias, K. B. Bourdakos, V. Jankus, K. C. Moss, K. T. Kamtekar, V. Bhalla, J. Santos, M. R. Bryce and A. P. Monkman, *Adv. Mater.*, 2013, **25**, 3707–3714.
8 C. Adachi, M. A. Baldo, M. E. Thompson and S. R. Forrest, *J. Appl. Phys.*, 2001, **90**, 5048–5505.
9 B. Zhao, T. Zhang, B. Chu, W. Li, Z. Su, Y. Luo, R. Li, X. Yan, F. Jin and Y. Gao, *Org. Electron.*, 2015, **17**, 15–21.
10 H. Uoyama, K. Goushi, K. Shizu, H. Nomura and C. Adachi, *Nature*, 2012, **492**, 234–238.
11 M. Y. Wong and E. Zysman-Colman, *Adv. Mater.*, 2017, **29**, 1605444.
12 T. Chen, L. Zheng, J. Yuan, Z. F. An, R. F. Chen, Y. Tao, H. H. Li, X. J. Xie and W. Huang, *Sci. Rep.*, 2015, **5**, 10923.
13 (*a*) R. Czerwieniec, J. Yu and H. Yersin, *Inorg. Chem.*, 2011, **50**, 8293–8301; (*b*) R. Czerwieniec and H. Yersin, *Inorg. Chem.*, 2015, **54**, 4322–4327.
14 J. Föller, M. Kleinschmidt and C. M. Marian, *Inorg. Chem.*, 2016, **55**, 7506–7516.
15 H. T. Sun, C. Zhong and J.-L. Brédas, *J. Chem. Theory Comput.*, 2015, **11**, 3851–3858.
16 J. Autschbach and M. Srebro, *Acc. Chem. Res.*, 2014, **47**, 2592–25602.
17 D. J. Tozer, *J. Chem. Phys.*, 2003, **119**, 12697–12699.
18 T. Körzdörfer and J. L. Brédas, *Acc. Chem. Res.*, 2014, **47**, 3284–3291.
19 S. P. Huang, Q. S. Zhang, Y. Shiota, T. Nakagawa, K. Kuwabara, K. Yoshizawa and C. Adach, *J. Chem.Theory. Comput.*, 2013, **9**, 3872–3877.
20 U. Salzner and A. Aydin, *J. Chem. Theory Comput.*, 2011, **7**, 2568–2583.
21 T. Stein, L. Kronik and R. Baer, *J. Am. Chem. Soc.*, 2009, **131**, 2818–2820.
22 S. Refaely-Abramson, S. Sharifzadeh, M. Jain, R. Baer, J. B. Neaton and L. Kronik, *Phys. Rev. B*, 2013, **88**, 081204.
23 (*a*) H. T. Sun, S. Ryno, C. Zhong, M. K. Ravva, Z. R. Sun, T. Körzdörfer and J.-L. Brédas, *J. Chem. Theory Comput.*, 2016, **12**, 2906–2916; (*b*) Z. Hu, B. Zhou, Z. R. Sun and H. T. Sun, *J. Comput. Chem.*, 2017, **38**, 569–575.
24 Q. Peng, Y. P. Yi, Z. G. Shuai and J. S. Shao, *J. Chem.Phys.*, 2007, **126**, 114302.
25 Y. L. Niu, Q. Peng, C. M. Deng, X. Gao and Z. G. Shuai, *J. Phys. Chem. A*, 2010, **114**, 7817–7831.
26 Q. Peng, Y. L. Niu, Q. Shi, X. Gao and Z. G. Shuai, *J. Chem. Theory Comput.*, 2013, **9**, 1132–1143.
27 Y. L. Niu, W. Q. Li, Q. Peng, H. Geng, Y. P. Yi, L. J. Wang, G. J. Nan, D. Wang and Z. G. Shuai, *Mol. Phys.*, 2018, **116**, 1078–1090.

28 L. L. Lv, K. Yuan and Y. C. Wang, *Org. Electron.*, 2017, **51**, 207–219.
29 L. L. Lv, K. Yuan and Y. C. Wang, *Phys. Chem. Chem. Phys.*, 2018, **20**, 6548–6561.
30 T. Yanai, D. P. Tew and N. C. Handy, *Chem. Phys. Lett.*, 2004, **393**, 51–57.
31 A. E. Raeber and B. M. Wong, *J. Chem. Theory Comput.*, 2015, **11**, 2199–2209.
32 M. A. Rohrdanz, K. M. Martins and J. M. Herber, *J. Chem. Phys.*, 2009, **130**, 054112.
33 D. A. Egger, S. Weismann, S. Refaely-Abramson, S. Sharifzadeh, M. Dauth, R. Baer, S. Kummel, J. B. Neaton, E. Zojer and L. Kronik, *J. Chem. Theory Comput.*, 2014, **10**, 1934–1952.
34 T. Lu, *optDFTw and scanDFTw program v1.0*, https://sobereva.com/346, (2017-3-8).
35 M. J. Frisch, G. W. Trucks and H. B. Schlegel, *et al.*, *Gaussian 09, Revision-D.01*, Gaussian Inc, Wallingford, CT, 2009.
36 S. Hirata and M. Head-Gordon, *Chem. Phys. Lett.*, 1999, **314**, 291–299.
37 T. Lu and F. Chen, Multiwfn: a multifunctional wavefunction analyzer, *J. Comput. Chem.*, 2012, **33**, 580–592.
38 K. Sugisaki, K. Toyota, K. Sato, D. Shiomi and T. Takui, *J. Phys. Chem. A*, 2016, **120**, 9857–9866.
39 F. Neese, The ORCA program system, *Wiley Interdiscip. Rev.: Comput. Mol. Sci.*, 2012, **2**, 73–78.
40 M. Roemelt and F. Neese, *J. Phys. Chem. A*, 2013, **117**, 3069–3083.
41 B. Minaev, G. Baryshnikov and H. Agren, *Phys. Chem. Chem. Phys.*, 2016, **16**, 1719–1758.
42 G. Baryshnikov, B. Minaev and H. Ågren, *Chem. Rev.*, 2017, **117**, 6500–6537.
43 T. J. Penfold, E. Gindensperger, C. Daniel and C. M. Marian, *Chem. Rev.*, 2018, DOI: 10.1021/acs.chemrev.7b00617.
44 Q. Peng, D. Fan, R. H. Duan, Y. P. Yi, Y. L. Niu, D. Wong and Z. G. Shuai, *J. Phys. Chem. C*, 2017, **121**, 13448–13456.
45 R. Czerwieniec, M. J. Leitl, H. H. H. Homeier and H. Yersin, *Coord. Chem. Rev.*, 2016, **325**, 2–28.
46 J. R. Kirchhoff, R. E. Gamache Jr, M. W. Blaskie, A. A. Del Paggio, R. K. Lengel and D. R. McMillin, *Inorg. Chem.*, 1983, **22**, 2380–2384.
47 P. K. Samanta, D. Kim, V. Coropceanu and J.-L. Brédas, *J. Am. Chem. Soc.*, 2017, **139**, 4042–4051.